MIT Open Access Articles

Nano-Scale Elastic Properties Due to Montmorillonite Water Adsorption

Massachusetts Institute of Technology

Nano-Scale Elastic Properties Due to Montmorillonite Water Adsorption

Davoud Ebrahimi[†], Roland J.-M. Pellenq[†‡,∗], Andrew J. Whittle[†]

[†]Department of Civil and Environmental Engineering

Massachusetts Institute of Technology, Cambridge, MA 02139, USA

[‡]Centre Interdisciplinaire de Nanosciences de Marseille, Aix-Marseille Université,

CNRS, Campus de Luminy, 13288 Marseille Cedex 09, France

Abstract

Smectites are an important group of clay minerals that experiences swelling upon water adsorption. This paper uses molecular dynamics with the CLAYFF force field to simulate isothermal isobaric water adsoption of interlayer Wyoming Na-montmorillonite, a member of the smectite group. Nano-scale elastic properties of the clay-interlayer water system are calculated from the potential energy of the model system. The transverse isotropic symmetry of the elastic constant matrix was assessed by calculating Euclidean and Riemannian distance metrics. Simulated elastic constants of the clay mineral are compared with available results from acoustic and nanoindentation measurements.

Keywords: molecular simulation, clay mineral adsorption, clay swelling, mechanical properties

* Author to whom correspondence should be addressed. E-mail: pellenq@mit.edu.

1 Introduction

The engineering properties of soils are highly affected by their clay content[1,2]. Similarly, the hydration state of the clay mineral plays an important role in physical properties such as the mechanics and transport of ionic substances. This work is motivated by the lack of a universal constitutive model to explain the effect of water adsorption on clay behavior (i.e., from partially saturated clay to fully saturated states). The fundamental understanding of the clay hydration process impacts several application fields from engineering estimates of ground movements caused by seasonal changes in moisture content to swelling pressures exerted by compacted bentonite on nuclear waste canisters.[3] Knowledge of elastic properties is critical in back-analyzing geophysical seismic exploration data and interpreting acoustic scattering measurements.[4] Fundamental mechanical properties of clays are also required to model hydraulic fracturing of oil and gas shale source rocks.[5] Clays are being used to improve mechanical and thermal properties of polymers, via polymer clay nanocomposites (PCNs).[6] These applications also require knowledge of fundamental properties of clay to design properties of the PCN composite materials.

Clay minerals have a layered structure at the nano-scale. Each layer consists of some combinations of two sheet types with silicon tetrahedra and aluminum octahedra as basic units. This work considers montmorillonite, a member of the smectite group that comprises two tetrahedral silicate sheets each with unshared oxygen, O, atoms around a central octahedral hydroxide sheet which has two planes of unshared O atoms and additional hydroxyl groups, OH, to form the base lamellae. Due to isomorphous substitutions of metal ions within the clay sheets, each lamellae has a net negative charge which is compensated by positive exchangeable interlayer cations. Adsorption of water molecules by this system is accompanied by a large increase in the basal layer spacing. This swelling process significantly impacts the structural and mechanical properties of the clay.

It is very challenging to measure the fundamental mechanical properties of clay due to their high affinity for water and their platy geometry.[7] Plan dimensions of each lamellae are typ-

ically one hundred times larger than the 2:1 layer thickness. All of the reported direct measurements are for clay minerals that are dry or have a very small amount of water (often ill-defined). Most of the available experimental results report only isotropic elastic moduli of clay minerals[8–12]. However, clay minerals have inherent anisotropy due to their layered structure as shown experimentally in the case of muscovite mica, phlogopite and biotite[13–15]. For example, Vanorio et al.[7] reported isotropic elastic moduli of montmorillonite samples from extrapolation of acoustic measurements on cold-pressed samples at different porosities but with no control of water content. Similarly, Wang et al.[16] presented a method to calculate elastic properties of clay from elastic wave velocity measurements on composite samples prepared by mixing the clay with an epoxy resin of known elastic properties. Chen and Evans[17] argued that this method does not necessarily measure the moduli of individual clay platelets.

To the best of our knowledge, successful direct anisotropic experimental measurements on montmorillonite mineral are currently not available in the literature, so theoretical and computational methods can provide useful estimates of these properties.
Molecular simulation is a computational technique that is used to model behavior of the matter at atomic scale. The existing literature on molecular simulation of clay water systems has focused on crystalline swelling behavior of the clay and on the interlayer distribution of water and ion molecules.[18–27]. There are very few reported elastic properties for clay minerals from numerical simulations. Most of the reported elastic moduli from computer simulations are for non-expanding minerals with small interlayer spacing. For example, Sato et al.[28] reported the first principle calculation of the full elastic stiffness matrix of kaolinite, a non expanding clay with small adsorption of water. Recently, Militzer et al.[29] reported the first principle ab initio calculations of full elastic stiffness constants for dry silicate minerals including muscovite, kaolinite, dickite, nacrite as well as a dry illite-smectite mineral. Suter et al.[30] and Mazo et al.[31] calculated in-plane elastic moduli of hydrated Wyoming Na-montmorillonite clay.

This paper derives the full elastic tensor calculations for Wyoming Na-montmorillonite over a range of hydration conditions using Molecular Dynamics (MD) simulations.

2 Methodology

The crystallography for 2:1 clay mineral has been taken from Refson et al.[32]. The specific structure of Wyoming Na-montmorillonite includes isomorphous substitutions in both tetrahedral and octahedral sheets with the following experimental formula: $Na_{0.75}nH_2O[Si_{7.75}Al_{0.25}]$ $[Al_{3.5}Mg_{0.5}]O_{20}(OH)_4$. The isomorphous substitutions in Wyoming Na-montmorillonite corresponds to cation exchange capacity of $102 \frac{meq}{100gr}$. The simulation cell consists of sixteen unit cell ($4\times2\times2$ array of clay unit cell) with initial plan dimensions ($X - Y$) of ~20.87 Å× ~18.15 Å. Sodium ions, Na,were randomly distributed in the interlayer space. Each simulation contains between 0 to 258 water molecules that corresponds to water contents in the range M_{H_2O}/M_{clay}= 0 to 0.4 g/g.

The analyses are based on the CLAYFF[33] force field that has been developed successfully for structural simulation of clay minerals[30,34]. CLAYFF is a versatile force field built around the flexible version of the simple point charge (SPC) water model[35]. All parameters and equations are given in the supporting information.

Two simulation packages were used in this work: GROMACS[36] and GULP[37]. GRO-MACS was used for molecular dynamics simulations while GULP was used to create the initial structure of the adsorbed water, to perform static energy minimization and to calculate the elastic stiffness matrix. The visualization of the molecular configurations was carried out using the molecular graphic software VMD[38]. The initial state of the adsorbed water was generated through Grand Canonical Monte Carlo (GCMC - μ-V-T) simulations at 300K. Three-dimensional, periodic boundary conditions were applied along with the min-

3

imum image convention (a cutoff radius of 8.5Å was used for short range interactions). The long range electrostatic coulombic interactions were calculated using Particle Mesh Ewald summation[39,40].

Isomorphous substitution was carried out randomly by replacing one Si^{4+} with Al^{3+} in each tetrahedral sheet, and four Al^{3+} with Mg^{2+} in each octahedral sheet. The resulting negative charge was compensated with sodium ions between the clay layers. This type of substitusion strategy was also used by Abdolhosseini Qomi et al.[41] to study the effect of elemental substitution on elastic properties of calcium- silicate-hydrate (CSH)- another mineral with layered structure. We carried out two different random isomorphous substitutions in the octahedral layer and created two distinct atomic structures for the computer simulations. Figure 1 shows the radial distribution functions of Mg-Mg defects of the two structures. In simulation(1), the two defects have a separation greater than 7.9Å , while in simulation(2) they are separated by more than 5.2Å. Figure 2 shows the typical structure of the simulated clay-water system. Clay swelling was simulated at an isothermal temperature, T=300 K, and isobaric pressure, P=0 GPa, using NPT ensemble over a time period, Δ t=900 ps (pico second). The Nosé–Hoover thermostat[42,43] is used to control temperature together with the Parrinello–Rahman[44] barostat to control pressure in the system. All properties are calculated from the last 500 ps of the simulations when the system has reached its equilibrium state. An integration time step of 1 fs (femto second) was used in all simulations.

2.1   Calculation of Elastic Properties

The single crystalline elastic stiffness properties were calculated using energy minimization of the structure obtained from MD simulation in GULP program. We use the Voigt notation in representing components of the fourth order elasticity tensor C_{ijkl} that changes the indices in the following way: 11→1, 22→2, 33→3, 23→4, 13→5 and 12→6. In this notation, fourth order elasticity tensor can be represented by a symmetrical matrix with components C_{ij}. We
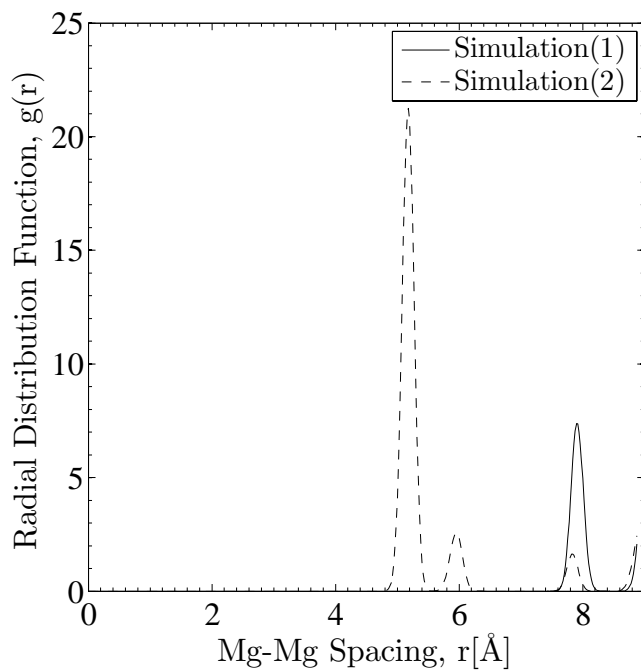
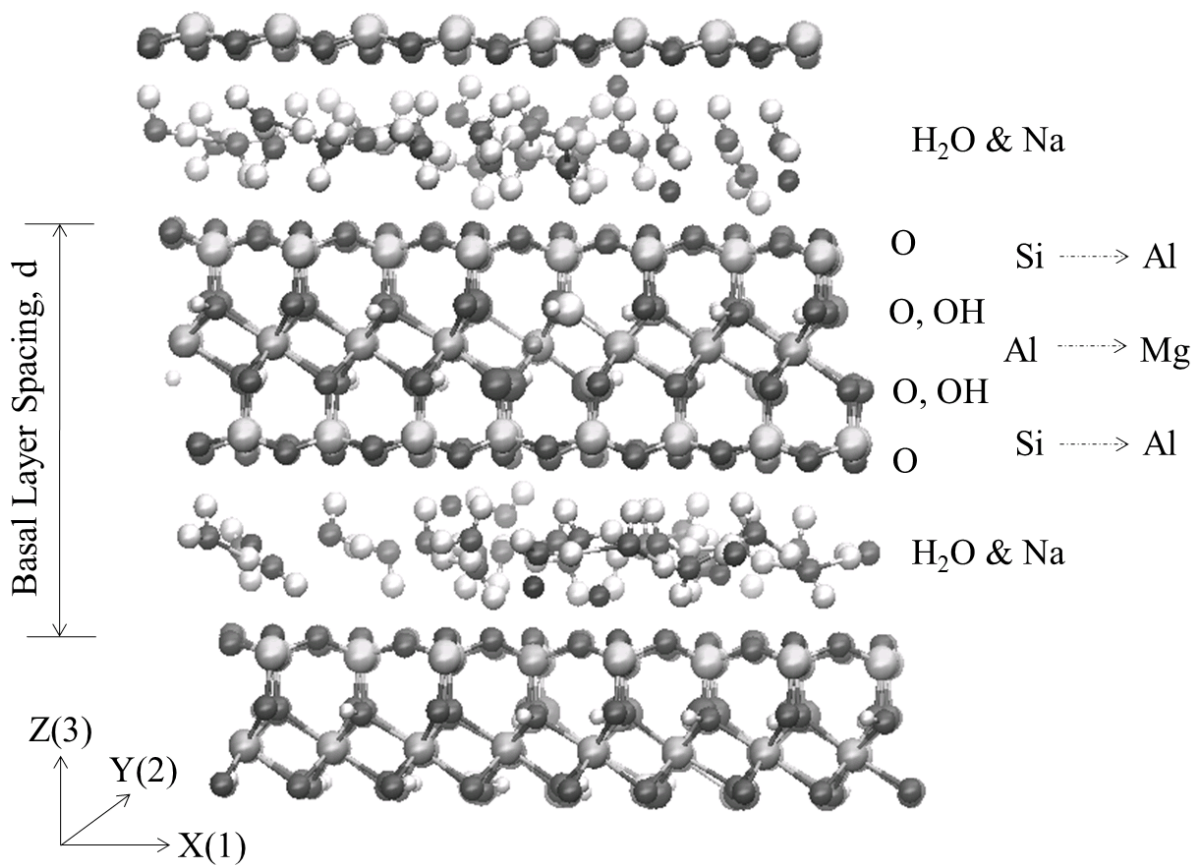Figure 1: Mg-Mg radial distribution functions of two atomic structures used in simulations.

Figure 2: Typical unit cell in periodic crystal of the simulated clay mineral at d=12Å.

will use cartesian coordinate system with direction 3 as the one normal to the clay layers(Z) and directions 1 and 2 in the plane of the clay layer(XY)(see Figure 2). The stiffness matrix C is defined as the second derivative of the potential energy with respect to strain:

$$C_{ij} = \frac{1}{\Omega} \frac{\partial^2 U}{\partial \epsilon_i \partial \epsilon_j} \qquad i, j = 1, 2, \ldots, 6 \tag{1}$$

where Ω is the volume of the unit cell, ϵ_1, ϵ_2 and ϵ_3 are the longitudinal strains in the X, Y and Z directions and ϵ_4, ϵ_5 and ϵ_6 are the shear strains in the YZ, XZ and XY planes, respectively. Energy minimization was accomplished using the BFGS steepest descent[45] algorithm. It should be noted that the minimizer switched to a Rational Function Optimization(RFO) algorithm[46] when the gradient norm fell below $5 \times 10^{-3} \frac{eV}{A}$. The RFO approach guarantees to find configurations with positive definite stiffness matrix which corresponds to a stable minimum. A similar procedure has been used to find equilibrium structure at the extrema of the energy surface with positive curvature for other layered minerals[41,47–49].

3 Results and Discussion

3.1 Hydration Mechanism

Cygan et al.[33] have shown very good agreement between numerical simulation and experimental measurements of swelling reported by Fu et al.[50] (i.e. basal layer spacing versus water content) for Wyoming Na-montmorillonite as part of the original validation of the CLAYFF[33] force field. We have performed a similar validation as part of the study (see supporting information). The mechanism of swelling can be explained by considering the average number of hydrogen bonds per water molecule and the density of the interlayer water as a function of the basal layer spacing, d, as shown in Figure 3. We have used the common geometric definition of hydrogen bond[51] in calculating the number of hydrogen bonds that each water molecule creates with surrounding water molecules. A hydrogen bond is assigned
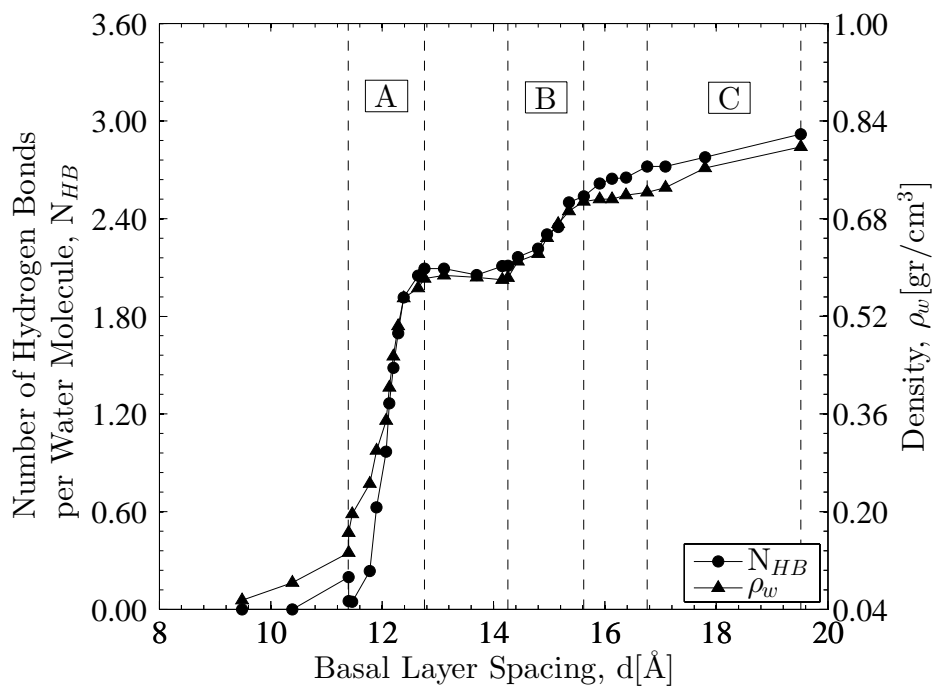
6

Figure 3: Change in average number of hydrogen bonds per water molecule and density of interlayer water during swelling of Wyoming Na-montmorillonite.
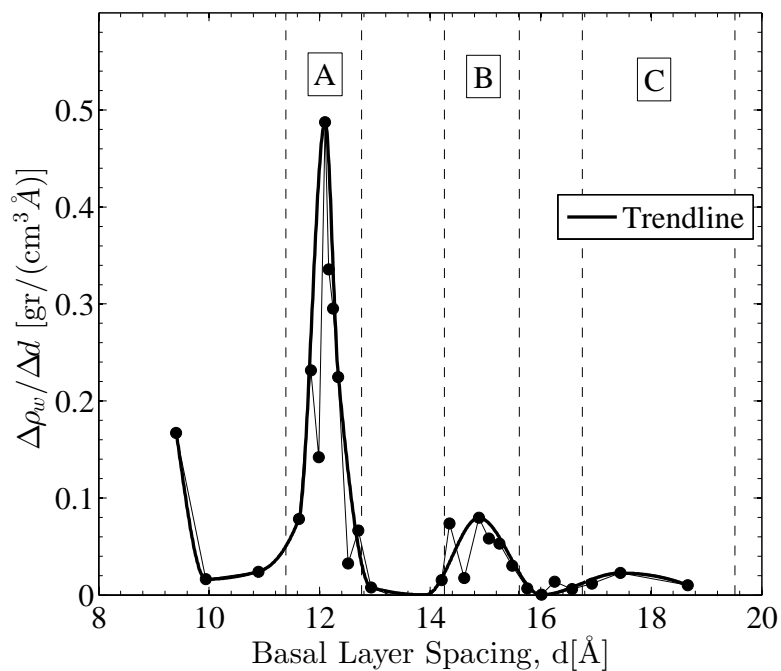

Figure 4: Change in derivative of the density with respect to basal layer spacing during swelling of Wyoming Na-montmorillonite.

when the O-O distance is less than 3.5Å and simultaneously the H-O-O angle is less than 30°. The average number of hydrogen bonds per water molecule at 300K in bulk water is 3.6 which corresponds to the density of $1\frac{gr}{cm^3}$. Three regions are identified in Figure 3: In region A, the density of the interlayer water (ρ_w) and number of hydrogen bonds (N_{HB}) increase rapidly to a threshold condition at d≈12.8 Å corresponding to the formation of mono-layer water-clay system. In transition from region A to B, the density of water and number of hydrogen bonds remains constant which indicates that the rate of water adsorption and increase in basal layer spacing are (almost) the same until the system reaches region B. Region B, d≈14.3-15.6 Å, corresponds to the formation of the second water layer. The transition from B to C is identified by the change in slope of both ρ_w and N_{HB}. Figure 4 shows the derivative of water density with respect to the basal layer spacing with maxima at d≈ 12Å and 15Å . We will show that these also correspond to maxima in some of the elastic stiffness constants. The formation of the third water layer (region C) is less visible. Figure
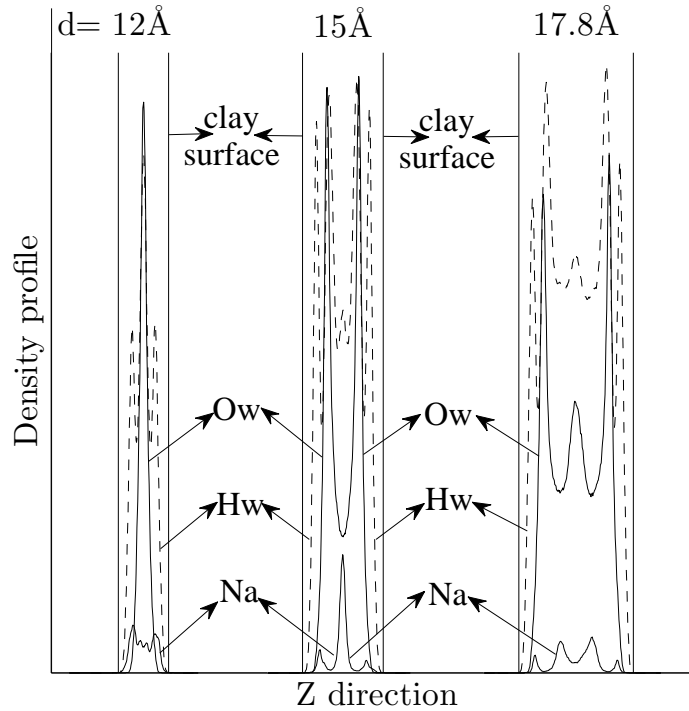

Figure 5: Density profile of water oxygen(Ow) and water hydrogen(Hw) and sodium(Na) in the direction normal to the clay layers.

5 shows the density profile for interlayer species in the direction normal to the clay layers for three different basal layer spacings (d≈12, 15 and 17.8 Å). These results show clearly the formation of the first, second and third layer of water molecules between clay sheets from the number of peaks in the water oxygen, Ow, distribution. For the two layer system (d≈15Å),the water molecules are distributed evenly between layers while for the three layer system there are more water molecules close to the clay surfaces than in the middle layer. Following Sposito et al.[52] the adsorption of interlayer cations in smectite can be classified as 'inner-sphere' or 'outer-sphere' complexes. Inner-sphere surface adsorption describes the condition where there is no water molecule between the cation and the clay surface, while an outer-sphere surface adsorption has at least one water molecule between the cation and the clay sheet. Formation of these surface complexes depends on both the charge and size of the cations and the location of the charged sites due to substitutions in clay layers[20,53]. For Wyoming Na-montmorillonite which has isomorphous substitutions in both tetrahedral and octahedral layers and (Na) cations as charge compensating ions, we expect to find formation of both inner and outer sphere complexes[52]. Our simulation results show that upon increasing water content, Na ions become more hydrated and detached from the clay surface[54]. Figure 5, confirms the formation of inner-sphere complexes by having peaks in (Na) cation distributions closer than peaks in (Ow) for all basal layer spacings. For d≈15Å through 17.8Å, there is a high concentration of Na-ions in the middle water layer. This shows an increase in outer-sphere complexes in agreement with Chávez-Páez et al.[55]. It should be noted that in our simulations, tetrahedral charge sites represent only 33 percent of the total clay layer charge. This explains the decrease of the number of inner-sphere complexes, as hydration proceeds. One can expect a different situation with a larger number of inner-complexes for a pure tetrahedrally substituted clay (the layer charge being then localized very close to the clay layer surface). The type of substitution (tetrahedral/octahedral layer) and the amount of substitutions define the resulting ion distribution that in turn affects the mechanical properties of the material in terms of the layer-to-layer cohesive pressure as

shown with primitive model simulations[56].

3.2 Elasticity

For each hydration state, the full elastic stiffness tensor ($[C_{ij}]$ $i, j = 1, 2, \ldots, 6$) has been calculated. It is usually desirable to approximate the full tensor (with 21 independent parameters) using assumptions of material symmetry. For a stack of clay lamellae, we expect good approximations with an equivalent transversely isotropic tensor composed of five independent engineering elastic constants : E_p, E_z, G_{pz}, ν_p and ν_{zp}. E_p and E_z are the Young's moduli in the plane of the basal layer and in the direction normal to it; G_{pz} is the shear modulus in planes normal to the isotropic plane; ν_p and ν_{zp} are the Poisson's ratios characterizing the lateral strain response in the plane of transverse isotropy to a stress acting parallel and normal to the isotropic plane. Values of the elastic constants of the transversely isotropic plane are calculated by averaging over x and y directions and over the two sets of simulations (denoted as $[\overline{C}_{ij}]$).

In the following discussion, we will show the variation of elastic stiffness constants C_{11} (and C_{22}), C_{33}, C_{44} (and C_{55}), C_{12}, C_{13} (and C_{23}) as a function of the degree of hydration for two structures with different locations of isomorphous substitutions. These constants can be directly related to the above listed set of engineering elastic constants. The mean and standard deviation between two simulation results will be reported.

Figure 6 shows the variations of C_{33} upon hydration. There is a sudden decrease in the mean value from $\overline{C}_{33} = 48.5 \pm 3.8$ GPa to 16.8 ± 1.2 GPa from the dry state to the mono layer hydration. The modulus increases upon further water adsorption to a local maximum, $\overline{C}_{33} = 30.0 \pm 0.5$ GPa at d$\approx$12Å (middle of region A). As the basal layer expands to accommodate more water molecules, there is a decrease in $\overline{C}_{33}$ (to 20.7 ± 2.3GPa at d$\approx$14Å), until region B. Formation of the second layer of water is associated with another local maximum, $\overline{C}_{33} = 26.2 \pm 3.0$GPa at d$\approx$15Å (middle of region B). Further increase in basal layer spacing has
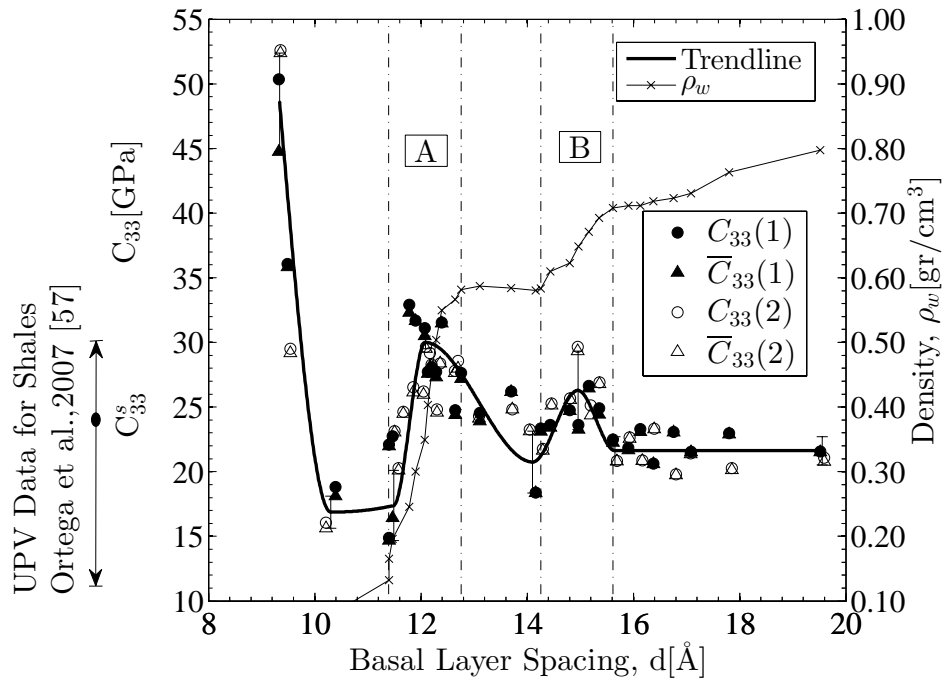
Figure 6: The C_{33} elastic constant as a function of basal layer spacing. Filled symbols represent data points from simulation (1) and hollow symbols represent data points from simulation (2). Triangular symbols represent equivalent transversely isotropic stiffness constants.

only a small impact on the modulus with $\overline{C}_{33}$= 21.6±1.08 GPa for d ≥ 15.6Å.

Ortega et al.[57] reported values of the elastic stiffness constants of the clay phase of the shale samples by back analyzing Ultrasonic Pulse Velocity (UPV) measurements. The tested samples include higher amounts of illite, smectite and kaolinite and less amounts of other clay minerals like chlorite, glauconite, biotite. They have not reported relative humidity or basal layer spacing for the represented clay packs. The UPV measurements provide elastic properties for macroscopic porous clay-silt inclusion composite (at the μm length scale), refered to as the level II structure, scaling relations are then introduced to estimate the fundamental properties for the individual clay layers (level 0 solid clay denoted by C_{ij}^s). Ortega et al.[57] reported C_{33}= 11.5-30.4 GPa (level II) for a wide range of shale mineralogies and estimated C_{33}^s= 24.2 GPa. This result is in good agreement with our molecular dynamics simulation for d ≥ 10 Å , but generally underestimates the numerical data for dry clay (d ≤ 9.5 Å).

Figure 7 shows the variations of the computed stiffness components C_{44} and C_{55} upon hydration. These components relate to the shear modulus normal to the basal plane. Shear stiffness decreases rapidly with basal layer spacing from the dry state (with maximum $\overline{C}_{44}$=7.2±1.9GPa). Water acts as a lubricant to decrease the shear resistance as the system deviates from the dry state. During formation of the first layer of water in region A, there is a slight increase in shear stiffness with maximum $\overline{C}_{44}$=5.4±0.1GPa. In this region, the clay surface creates strong Coulombic bonding with the adsorbed water, confirming Sayers'[58] argument that water bounded to the clay surface may create an ordered structure with non-zero shear modulus. Between region A and region B, the shear stiffness remains approximately constant. During the formation of the second layer of water shear stiffness decreases slightly and reduces to a constant value $\overline{C}_{44}$=4.1±0.3GPa for d≥15.6Å. Ortega et al.[57] reported UPV (level II) measurements for clay shales of C_{44}=2.9-8.9GPa and intepreted the stiffness for the clay lamellae (level 0), C_{44}^s=3.7GPa. These values are generally in good
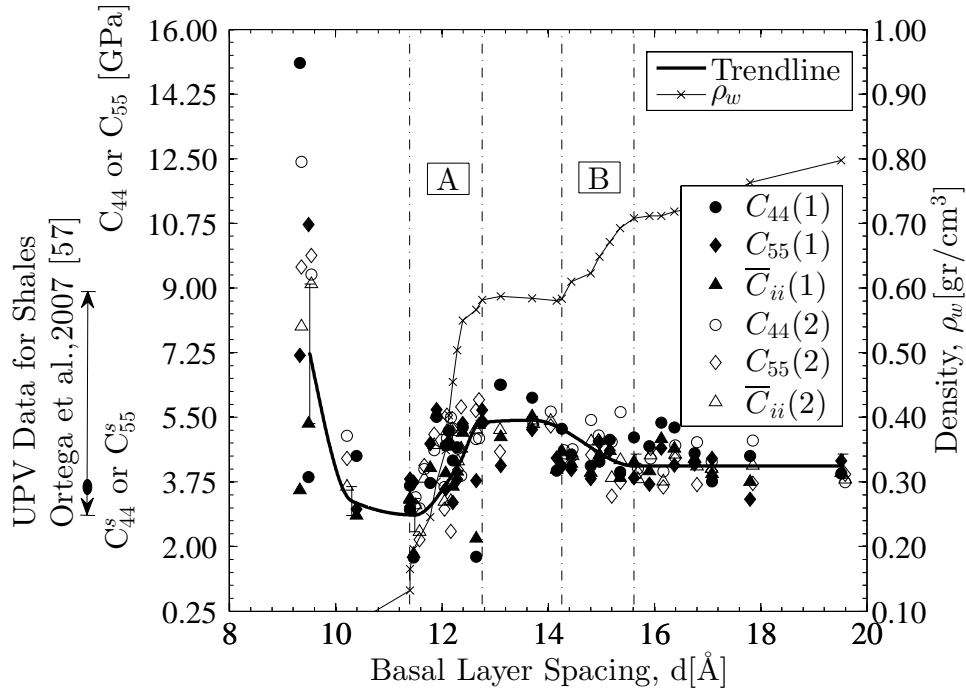
Figure 7: The C_{44} and C_{55} elastic constants as a function of basal layer spacing. Legend as in Figure 6.

agreement with the current numerical calculations for Wyoming Na-montmorillonite.

Figure 8 shows change in the C_{13} and C_{23} elastic components during hydration. The trend of the $\overline{C}_{13}$ is similar to $\overline{C}_{44}$, decreases from a dry state maximum, $\overline{C}_{13} = 18.0 \pm 1.6$GPa to 4.9 ± 0.6GPa, at region A, rising to a local maximum 9.7 ± 0.01GPa with a constant value 7.7 ± 0.6GPa for d$\geq$14.3Å. Ortega et al.[57] reported a wide range of C_{13} (6.1-24.3 GPa) from UPV tests and interpreted $C_{13}^s = 18.1$GPa for the clay lamellae. The C_{13} and C_{23} are related to the lateral Poisson's ratio connecting deformation between the vertical and horizontal axes. Although the fundamental stiffness component for the solid clay lamellae is consistent with the numerical simulations at small basal layer spacing, the UPV data are generally higher than the computed range for $\overline{C}_{13}$. This discrepancy may relate to effects of the finite aggregate size on UPV measurements, while the results of the molecular dynamics simulation corresponds to lamellae of infinite length.

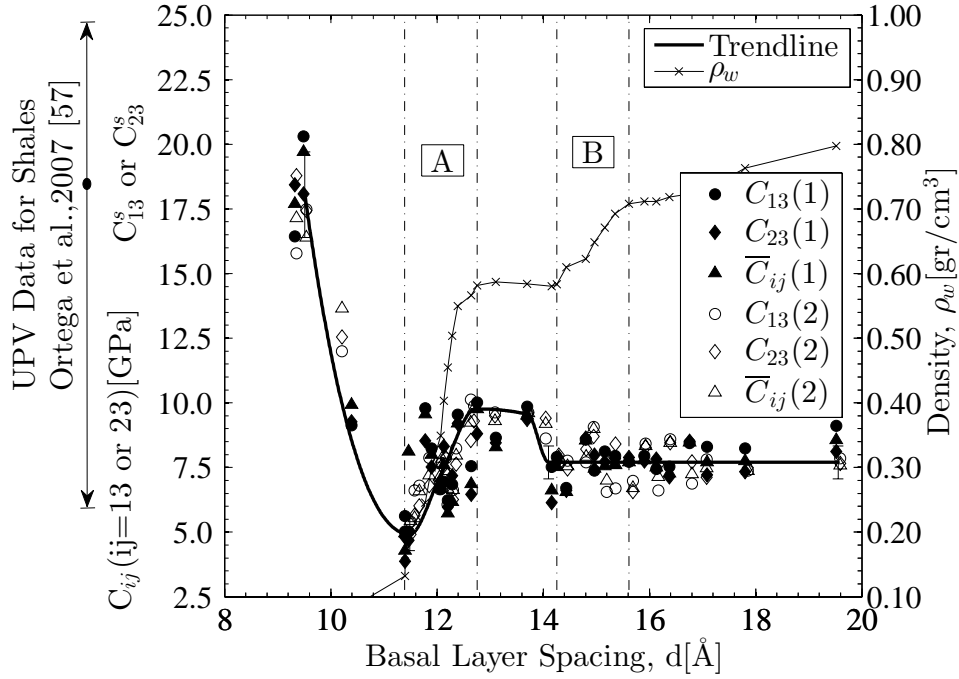The stiffness components C_{11}, C_{22} and C_{12} are mainly affected by the strong iono-covalent

Figure 8: The C_{13} and C_{23} elastic constants as a function of basal layer spacing. Legend as in Figure 6.
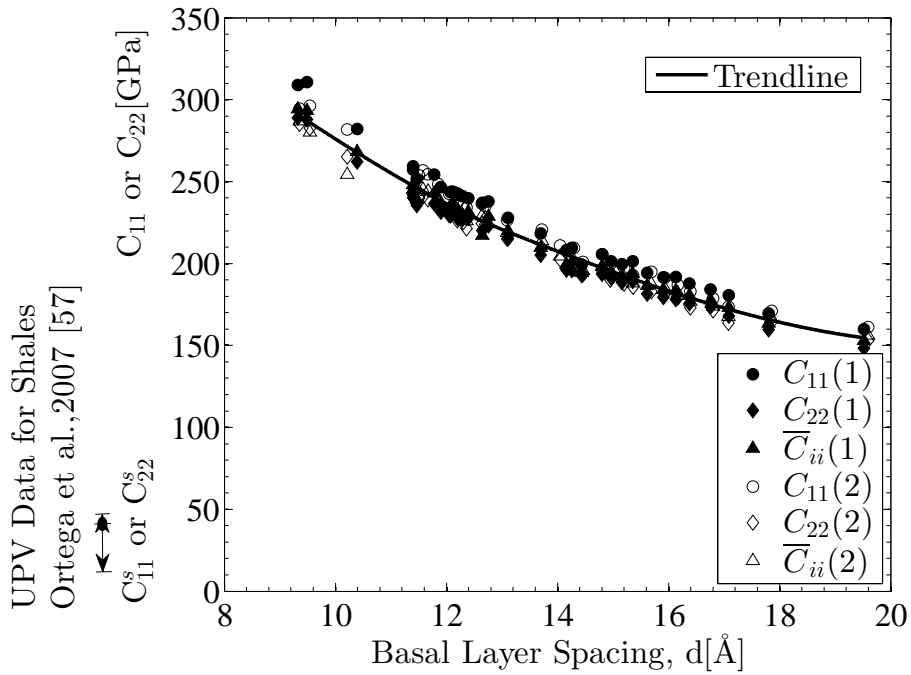

Figure 9: The C_{11} and C_{22} elastic constants as a function of basal layer spacing. Legend as in Figure 6.

bonding inside the clay layers. Figures 9 and 10 show the variations in C_{11}, C_{22} and C_{12} elastic constants during hydration. The C_{11} and C_{22} elastic constants represent Young's moduli in the plane of transverse isotropy. Both $\overline{C}_{11}$ and $\overline{C}_{12}$ continuously decrease by increasing basal layer spacing from 290.5±3.7GPa at d≈9.3 Å to 154.5±1.6GPa at d≈19.5Å. These values are 5 to 8 times larger than corresponding values in the direction normal to the clay layers. The large difference between C_{11} or C_{22} and C_{33} values comes from the difference between iono-covalent bonding inside the clay crystal layer and screened electrostatic bondings between layers. The average values of Young's moduli at d≈12Å are E_x=180GPa and E_y=172GPa that are in very good agreement with values from MD simulations by Suter et al.[30] (E_x=182GPa and E_y=172GPa) and Mazo et al.[31] (E_x=182GPa and E_y=180GPa). The computed results are much higher than the UPV data[57] (C_{11}=13.8-46.1GPa) and the calculated value for the clay lamellae[57] (C_{11}^s=44.9GPa). This discrepancy is almost certainly related to finite length of the clay aggregates affecting experimental measurements at the UPV scale (sliding between layers etc.)

Figure 10 shows the variation of stiffness component $\overline{C}_{12}$ upon hydration. The elastic constant $\overline{C}_{12}$ continuously decreases by increasing basal layer spacing from 140.8±3GPa at d≈9.3 Å to 77.6±1.5GPa at d≈19.5Å. Ortega et al.[57] reported UPV measurement of C_{12}=6.9-17.8GPa and calculated the stiffness for the clay lamellae C_{12}^s=21.7GPa[57] which is less than the values from MD simulation and can also be attributed to finite length effect in the clay aggregation.

Nano-indentation is one of the sub-micron experiments used to measure material stiffness parameters. To the best of our knowledge, there are no nanoindentation measurements on Wyoming Na-montmorillonite. However, Bobko and Ulm[59] performed a series of nanoindentation tests on the same shale samples analyzed by Ortega et al.[57]. By doing statistical analysis of the results, they extracted nanoindentation moduli for the clay phase. They
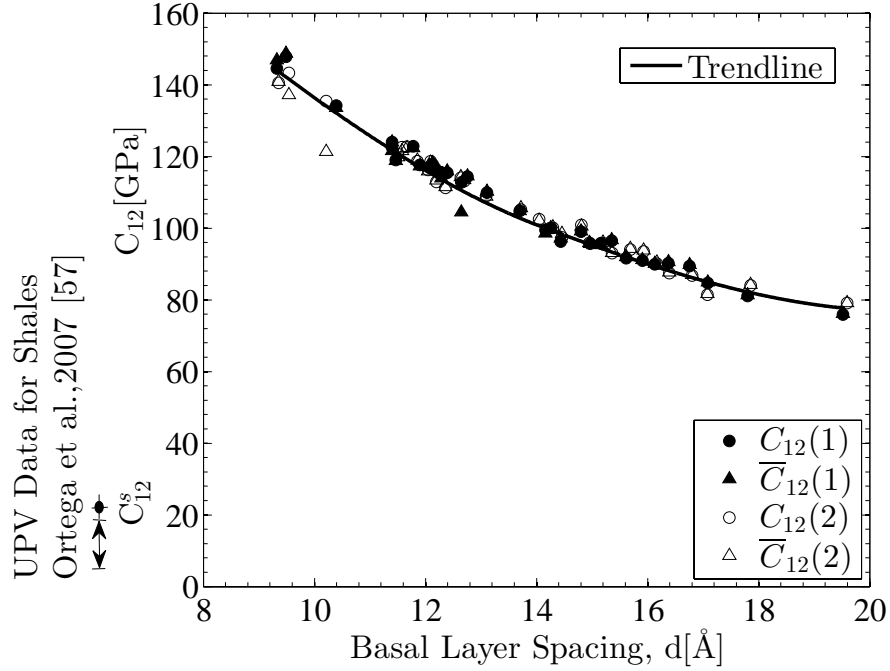
Figure 10: The C_{12} elastic constant as a function of basal layer spacing. Legend as in Figure 6.

carried out indentation measurements normal and parallel to the bedding plane defining M_z for indentation modulus normal to the bedding plane and M_p for the one parallel to the bedding plane. They reported solid phase nanoindentation moduli extrapolated to zero meso-scale porosity, $M_z^s = 16$GPa and $M_p^s = 25$GPa. Zhang et al.[60] have also reported a series of nanoindentation results on muscovite and rectorite. The atomic structure of rectorite consists of alternating sequence of fixed and expandable clay layers. They reported a range for the nanoindentation modulus of rectorite $M_z = 19.5 \pm 4.9$GPa. It should be noted that relative humidity is not controlled or measured during these tests. Indentation moduli can be computed from transversely isotropic stiffness components using the derivation by Delafargue and Ulm[61]:

$$M_z = 2\sqrt{\frac{C_{11}C_{33} - C_{13}^2}{C_{11}}\left(\frac{1}{C_{44}} + \frac{2}{\sqrt{C_{11}C_{33}} + C_{13}}\right)^{-1}} \qquad (2)$$

16

$$M_p \approx \sqrt{\sqrt{\frac{C_{11}}{C_{33}}} \frac{C_{11}^2 - C_{12}^2}{C_{11}} M_z} \qquad (3)$$
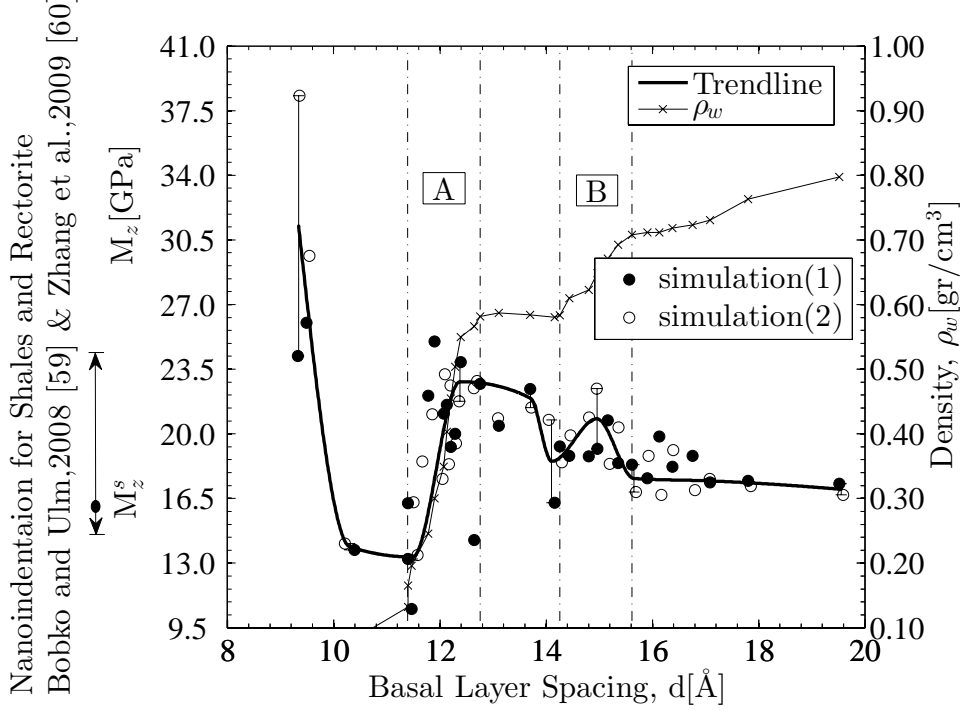

Figure 11: Indentation modulus in z direction as a function of basal layer spacing. Legend as in Figure 6.

Figures 11 and 12 show the computed naonindentation moduli of Wyoming Na-montmorillonite from molecular dynamics simulations using an equivalent transversely isotropic elastic stiffness matrix as functions of the basal layer spacing. Figure 11 shows that the variation of M_z is similar to change in C_{33} stiffness component (Figure 6). After a sudden decrease from $31.2 \pm 7.0 GPa$ to $13.3 \pm 0.1 GPa$ for d≈9Å to 11.5Å , there are local maxima $22.8 \pm 1.1 GPa$ at d≈12Å and $20.8 \pm 1.6 GPa$, at d≈15 Å. For d≥15.6Å the M_z value is approximately constant $(17 \pm 0.3 GPa)$. Results of the simulations are in very good agreement with the nanoindentation experiments[59,60] from region B onward to larger basal layer spacing.

Figure 12 shows the modulus parallel to the basal planes M_p decreases from $133.5 \pm 6.2 GPa$ (d≈9.3Å) to $96.5 \pm 3.4 GPa$(d≈11.5Å). There is a small increase to $106.0 \pm 0.2 GPa$ at region A which corresponds to the building up of the first water layer which has strong interac-
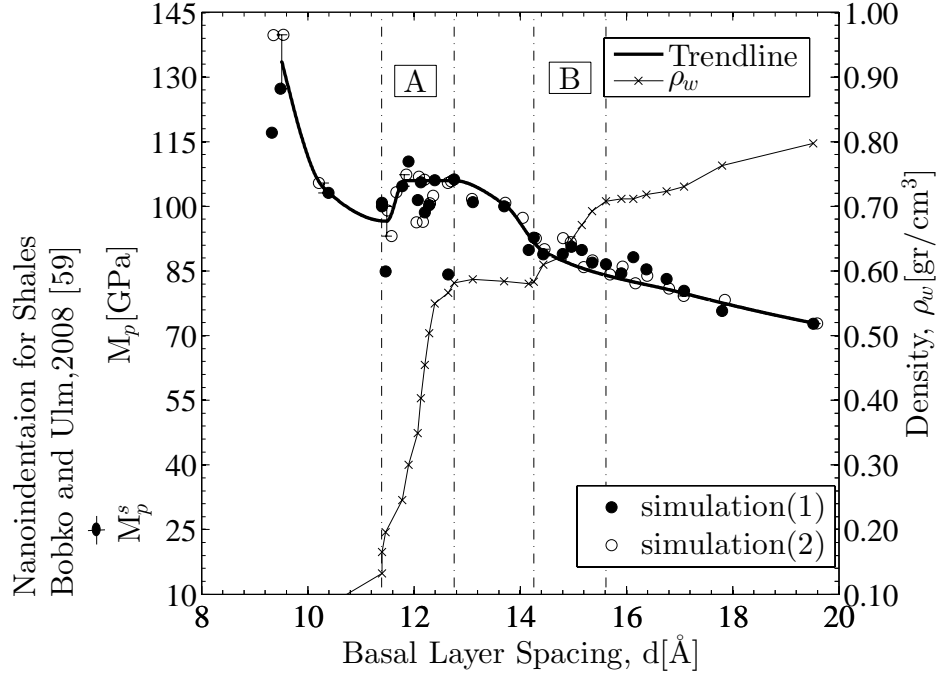
Figure 12: Indentation modulus in the plane of transverse isotropy as a function of basal layer spacing. Legend as in Figure 6.

tion with the clay surface. After region A, M_p continuously decreases to 72.8 ± 0.03GPa at d$\approx$19.5Å. The experimental estimates for clay plates, $M_p^{s\,59}$ is much smaller than our simulated values. This difference can be explained by the fact that nanoindentation parallel to the clay layers measures elastic stiffness due to sliding of finite clay layers against each other (similar to C_{11}, C_{22} and C_{12}) and not the stiffness of infinitely long clay layers as modeled in MD simulation.

Following the methodology of Shahsavari et al.[62], the Euclidean and Riemannian distance metrics are used to evaluate the accuracy of the equivalent transversely isotropic parameters $(\overline{C}_{ij})$ in representing the full elastic stiffness matrix (C_{ij}) of the clay-water system. The Euclidean distance metric is one of the most commonly used distance metrics[63] that relates two square matrices, $\mathbf{A_1}$ and $\mathbf{A_2}$, as follows:

$$d_E(\mathbf{A_1}, \mathbf{A_2}) = \|\mathbf{A_1} - \mathbf{A_2}\|_E \tag{4}$$

18

and the associated norm is defined by:

$$\|\mathbf{A}\|_E = \sqrt{tr\left(\mathbf{A}^T\mathbf{A}\right)} \tag{5}$$

where tr($\cdot$) stands for the trace and the superscript T denotes the transpose. The classical Euclidean distance metric is fast and easy to compute but lacks certain physically meaningful properties[64] and can generate symmetric matrices with null or negative eigenvalues. These problems are avoided using the Riemannian metric. The Riemannian metric is independent of the coordinate system, preserves material symmetries and is invariant under inversion[65]. Having two positive definite matrices, $\mathbf{P_1}$ and $\mathbf{P_2}$, the Riemannian metric is defined as follows:

$$d_R(\mathbf{P_1}, \mathbf{P_2}) = \left\| \ln\left(\mathbf{P_2}^{1/2}\mathbf{P_1}^{-1}\mathbf{P_2}^{1/2}\right) \right\|_R = \left[\sum_{i=1}^{n} \ln^2 \lambda_i\right]^{1/2} \tag{6}$$

where λ_i are the eigenvalues of $\mathbf{P_1}^{-1}\mathbf{P_2}$.

These metrics are means of measuring similarity between two matrices. For both metrics the smaller value means better approximation in representing full matrix with its equivalent transverse isotropic one.

Figures 13(a) and 13(b), show relative Euclidean and Riemannian distance metrics of full and transversely isotropic elastic stiffness matrices as a function of the basal layer spacing. The results shows that the transversely isotropic approximation is a good representation of elastic stiffness parameters for d$\geq$12Å, but becomes less reliable for conditions approaching the dry state.

4   Conclusion

This paper has presented a complete set of elastic stiffness constants for Wyoming Na-montmorillonite based on computational molecular dynamics simulations. The results show the variation in elastic constants as a function of the hydration state and basal layer spacing.
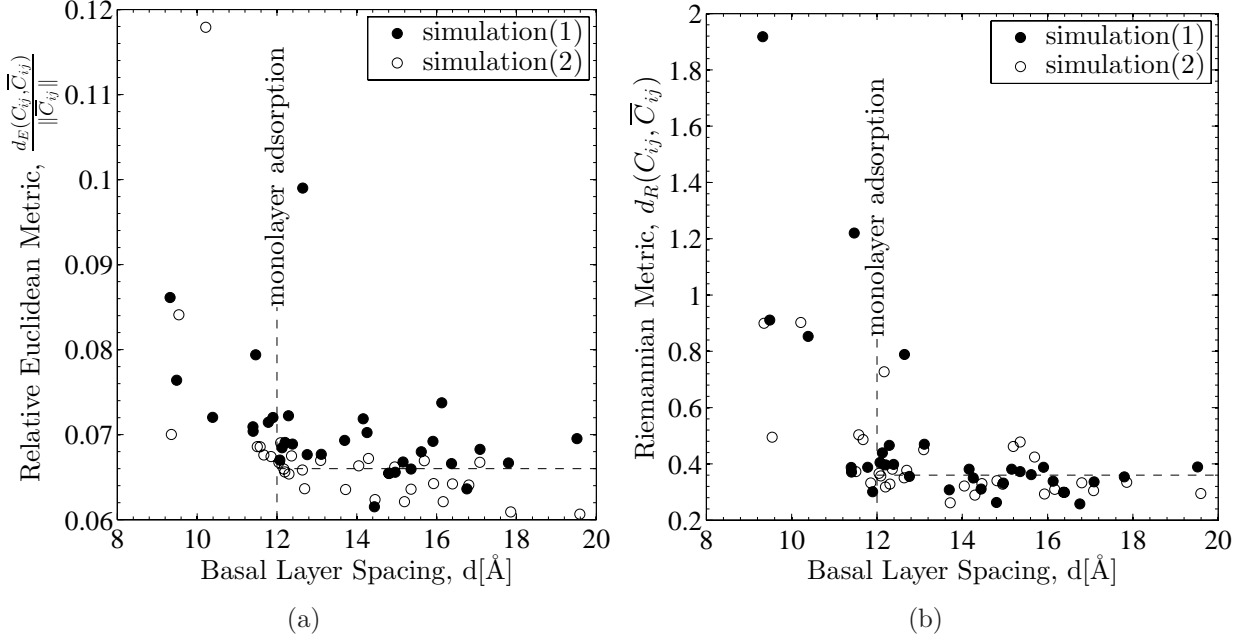
19

Figure 13: (a) Relative Euclidean Metric as a function of basal layer spacing. (b) Riemannian Metric as a function of basal layer spacing. Legend as in Figure 6.

Key findings for the individual stiffness components can be summarized as follows:

(1) The normal stiffness $\overline{C}_{33}$ oscillates with hydration level linked to the formation of mono and double layer of inter-lamellae water.

(2) The $\overline{C}_{33}$, $\overline{C}_{44}$(and $\overline{C}_{55}$) and M_z values are in good agreement with acoustic and nano-indentation experiments for basal layer spacing d$\geq$15.6Å corresponding to a system with two layers of water.

(3) The computed in-plane stiffness parameters $\overline{C}_{11}$(and $\overline{C}_{22}$), $\overline{C}_{12}$ and M_p (and to a less degree $\overline{C}_{13}$(and $\overline{C}_{23}$)) differ from the experimental measurements,. However the latter are illustrated by the finite length of clay particles while the current simulations represent conditions for infinitely long plates.

(4) Transverse isotropic assumption of mechanical properties for the clay mineral is a good approximation after the formation of the first layer of water but is less reliable for representing the dry state of the clay lamellae.

5   Acknowledgement

References

(1) H.H. Murray. Applied clay mineralogy today and tomorrow. *Clay Minerals*, 34(1):39, 1999.

(2) P. Boivin, P. Garnier, and D. Tessier. Relationship between clay content, clay type, and shrinkage properties of soil samples. *Soil Science Society of America Journal*, 68(4):1145–1153, 2004.

(3) A. Gens. The role of geotechnical engineering in nuclear energy utilisation (special lecture). In *Proc 13th Eur Conf Soil Mech Geotech Engng Prague*, volume 3, pages 25–67, 2003.

(4) Z.Z. Wang. Y2k tutorial: Fundamentals of seismic rock physics. *Geophysics*, 66(2):398–412, 2001.

(5) G. Waters, R. Lewis, and D. Bentley. The effect of mechanical properties anisotropy in the generation of hydraulic fractures in organic shales. In *SPE Annual Technical Conference and Exhibition*, 2011.

(6) S. SinhaRay and M. Biswas. Preparation and evaluation of composites from montmorillonite and some heterocyclic polymers: 3. a water dispersible nanocomposite from pyrrole-montmorillonite polymerization system. *Materials research bulletin*,

34(8):1187–1194, 1999.

(7) T. Vanorio, M. Prasad, and A. Nur. Elastic properties of dry clay mineral aggregates, suspensions and sandstones. *Geophysical Journal International*, 155(1):319–326, 2003.

(8) J. Faust and E. Knittle. Static compression of chondrodite: Implications for water in the upper mantle. *Geophysical Research Letters*, 21(18):1935–1938, 1994.

(9) A. Pavese, G. Ferraris, V. Pischedda, and M. Mezouar. Synchrotron powder diffraction study of phengite 3t from the dora-maira massif: P-v-t equation of state and petrological consequences. *Physics and chemistry of minerals*, 26(6):460–467, 1999.

(10) J.R. Smyth, S.D. Jacobsen, R.J. Swope, R.J. Angel, T. Arlt, K. Domanik, and J.R. Holloway. Crystal structures and compressibilities of synthetic 2m1 and 3t phengite micas. *European Journal of Mineralogy*, 12(5):955, 2000.

(11) A.R. Pawley, S.M. Clark, and N.J. Chinnery. Equation of state measurements of chlorite, pyrophyllite, and talc. *American Mineralogist*, 87(8-9):1172, 2002.

(12) M. Kopycinska-Müller, M. Prasad, U. Rabe, and W. Arnold. Elastic properties of clay minerals determined by atomic force acoustic microscopy technique. *Acoustical Imaging*, pages 409–416, 2007.

(13) M.T. Vaughan and S. Guggenheim. Elasticity of muscovite and its relationship to crystal structure. *Journal of Geophysical Research*, 91(B5):4657–4664, 1986.

(14) L.E. McNeil and M. Grimsditch. Elastic moduli of muscovite mica. *Journal of Physics: Condensed Matter*, 5:1681, 1993.

(15) K.S. Alexandrov and T.V. Ryzhova. Elastic properties of rock-forming minerals ii. layered silicates. *Bulletin of the Academy of Sciences of the USSR, Geophysics Series*, 12:1165–1168, 1961.

(16) Z.Z. Wang, H. Wang, and M.E. Cates. Effective elastic properties of solid clays. *Geophysics*, 66(2):428, 2001.

(17) B. Chen and J.R.G. Evans. Elastic moduli of clay platelets. *Scripta materialia*, 54(9):1581–1585, 2006.

(18) A. Delville. Structure of liquids at a solid interface: an application to the swelling of clay by water. *Langmuir*, 8(7):1796–1805, 1992.

(19) A. Delville and S. Sokolowski. Adsorption of vapor at a solid interface: a molecular model of clay wetting. *The Journal of Physical Chemistry*, 97(23):6261–6271, 1993.

(20) N.T. Skipper, G. Sposito, and F.R.C. Chang. Monte carlo simulation of interlayer molecular structure in swelling clay minerals. 2. monolayer hydrates. *Clays and Clay minerals*, 43(3):294–303, 1995.

(21) F.R.C. Chang, NT Skipper, and G. Sposito. Computer simulation of interlayer molecular structure in sodium montmorillonite hydrates. *Langmuir*, 11(7):2734–2741, 1995.

(22) D.E. Smith. Molecular computer simulations of the swelling properties and interlayer structure of cesium montmorillonite. *Langmuir*, 14(20):5959–5967, 1998.

(23) R.M. Shroll and D.E. Smith. Molecular dynamics simulations in the grand canonical ensemble: Application to clay mineral swelling. *The Journal of chemical physics*, 111:9025, 1999.

(24) V. Marry, P. Turq, T. Cartailler, and D. Levesque. Microscopic simulation of structure and dynamics of water and counterions in a monohydrated montmorillonite. *The Journal of chemical physics*, 117:3454, 2002.

(25) T.J. Tambach, E.J.M. Hensen, and B. Smit. Molecular simulations of swelling clay minerals. *The Journal of Physical Chemistry B*, 108(23):7586–7596, 2004.

(26) T.J. Tambach, P.G. Bolhuis, E.J.M. Hensen, and B. Smit. Hysteresis in clay swelling induced by hydrogen bonding: accurate prediction of swelling states. *Langmuir*, 22(3):1223–1234, 2006.

(27) V. Marry, B. Rotenberg, and P. Turq. Structure and dynamics of water at a clay

surface from molecular dynamics simulation. *Physical Chemistry Chemical Physics*, 10(32):4802–4813, 2008.

(28) H. Sato, K. Ono, C.T. Johnston, and A. Yamagishi. First-principles studies on the elastic constants of a 1: 1 layered kaolinite mineral. *American Mineralogist*, 90(11-12):1824, 2005.

(29) B. Militzer, H.R. Wenk, S. Stackhouse, and L. Stixrude. First-principles calculation of the elastic moduli of sheet silicates and their application to shale anisotropy. *American Mineralogist*, 96(1):125, 2011.

(30) J.L. Suter, P.V. Coveney, H.C. Greenwell, and M.A. Thyveetil. Large-scale molecular dynamics study of montmorillonite clay: Emergence of undulatory fluctuations and determination of material properties. *The Journal of Physical Chemistry C*, 111(23):8248–8259, 2007.

(31) M.A. Mazo, L.I. Manevitch, E.B. Gusarova, A.A. Berlin, N.K. Balabaev, and G.C. Rutledge. Molecular dynamics simulation of thermomechanical properties of montmorillonite crystal. ii. hydrated montmorillonite crystal. *The Journal of Physical Chemistry C*, 112(44):17056–17062, 2008.

(32) K. Refson, S.H. Park, and G. Sposito. Ab initio computational crystallography of 2: 1 clay minerals: 1. pyrophyllite-1tc. *The Journal of Physical Chemistry B*, 107(48):13376–13383, 2003.

(33) R.T. Cygan, J.J. Liang, and A.G. Kalinichev. Molecular models of hydroxide, oxyhydroxide, and clay phases and the development of a general force field. *The Journal of Physical Chemistry B*, 108(4):1255–1266, 2004.

(34) X. Liu, X. Lu, R. Wang, H. Zhou, and S. Xu. Interlayer structure and dynamics of alkylammonium-intercalated smectites with and without water: A molecular dynamics study. *Clays and Clay Minerals*, 55(6):554, 2007.

(35) O. Teleman, B. Jonsson, and S. Engstrom. A molecular dynamics simulation of a water

model with intramolecular degrees of freedom. *Molecular Physics*, 60(1):193–203, 1987.

(36) D. Van Der Spoel, E. Lindahl, B. Hess, G. Groenhof, A.E. Mark, and H.J.C. Berendsen. Gromacs: fast, flexible, and free. *Journal of computational chemistry*, 26(16):1701, 2005.

(37) J.D. Gale. Gulp: A computer program for the symmetry-adapted simulation of solids. *J. Chem. Soc., Faraday Trans.*, 93(4):629–637, 1997.

(38) W. Humphrey, A. Dalke, and K. Schulten. Vmd: visual molecular dynamics. *Journal of molecular graphics*, 14(1):33–38, 1996.

(39) T. Darden, D. York, and L. Pedersen. Particle mesh ewald: An n. log (n) method for ewald sums in large systems. *The Journal of Chemical Physics*, 98:10089, 1993.

(40) U. Essmann, L. Perera, M.L. Berkowitz, T. Darden, H. Lee, and L.G. Pedersen. A smooth particle mesh ewald method. *Journal of Chemical Physics*, 103(19):8577–8593, 1995.

(41) M.J. Abdolhosseini Qomi, F.J. Ulm, and R.J.M. Pellenq. Evidence on the dual nature of aluminum in the calcium-silicate-hydrates based on atomistic simulations. *Journal of the American Ceramic Society*, 95:1128–1137, 2012.

(42) S. Nosé. A unified formulation of the constant temperature molecular dynamics methods. *The Journal of chemical physics*, 81:511, 1984.

(43) W.G. Hoover. Canonical dynamics: Equilibrium phase-space distributions. *Physical Review A*, 31(3):1695, 1985.

(44) M. Parrinello and A. Rahman. Polymorphic transitions in single crystals: A new molecular dynamics method. *Journal of Applied Physics*, 52(12):7182–7190, 1981.

(45) W.H. Press, S.A. Teukolsky, W.T. Vetterling, and B.P. Flannery. Numerical recipes in c. 1992.

(46) A. Banerjee, N. Adams, J. Simons, and R. Shepard. Search for stationary points on

surfaces. *The Journal of Physical Chemistry*, 89(1):52–57, 1985.

(47) A.L. Auzende, R.J.M. Pellenq, B. Devouard, A. Baronnet, and O. Grauby. Atomistic calculations of structural and elastic properties of serpentine minerals: the case of lizardite. *Physics and chemistry of minerals*, 33(4):266–275, 2006.

(48) R.J.M. Pellenq, A. Kushima, R. Shahsavari, K.J. Van Vliet, M.J. Buehler, S. Yip, and F.J. Ulm. A realistic molecular model of cement hydrates. *Proceedings of the National Academy of Sciences*, 106(38):16102–16107, 2009.

(49) H. Manzano, E. Durgun, M.J. Abdolhosseini Qomi, F.J. Ulm, R.J.M. Pellenq, and J.C. Grossman. Impact of chemical impurities on the crystalline cement clinker phases determined by atomistic simulations. *Crystal Growth & Design*, 2011.

(50) M.H. Fu, Z.Z. Zhang, and P.F. Low. Changes in the properties of a montmorillonite-water system during the adsorption and desorption of water: hysteresis. *Clays and Clay Minerals*, 38(5):485–492, 1990.

(51) A. Luzar and D. Chandler. Effect of environment on hydrogen bond dynamics in liquid water. *Physical review letters*, 76(6):928–931, 1996.

(52) G. Sposito, N.T. Skipper, R. Sutton, S. Park, A.K. Soper, and J.A. Greathouse. Surface geochemistry of the clay minerals. *Proceedings of the National Academy of Sciences*, 96(7):3358, 1999.

(53) J. Greathouse and G. Sposito. Monte carlo and molecular dynamics studies of interlayer structure in li (h2o) 3-smectites. *The Journal of Physical Chemistry B*, 102(13):2406–2414, 1998.

(54) E.S. Boek, P.V. Coveney, and N.T. Skipper. Monte carlo molecular modeling studies of hydrated li-, na-, and k-smectites: Understanding the role of potassium as a clay swelling inhibitor. *Journal of the American Chemical Society*, 117(50):12608–12617, 1995.

(55) M. Chávez-Páez, K. Van Workum, L. De Pablo, and J.J. de Pablo. Monte carlo simula-

tions of wyoming sodium montmorillonite hydrates. *The Journal of Chemical Physics*, 114:1405, 2001.

(56) R.J.M. Pellenq, JM Caillol, and A. Delville. Electrostatic attraction between two charged surfaces: A (n, v, t) monte carlo simulation. *The Journal of Physical Chemistry B*, 101(42):8584–8594, 1997.

(57) J.A. Ortega, F.J. Ulm, and Y. Abousleiman. The effect of the nanogranular nature of shale on their poroelastic behavior. *Acta Geotechnica*, 2(3):155–182, 2007.

(58) C.M. Sayers. Seismic anisotropy of shales. *Geophysical prospecting*, 53(5):667–676, 2005.

(59) C. Bobko and F.J. Ulm. The nano-mechanical morphology of shale. *Mechanics of Materials*, 40(4-5):318–337, 2008.

(60) G. Zhang, Z. Wei, and R.E. Ferrell. Elastic modulus and hardness of muscovite and rectorite determined by nanoindentation. *Applied Clay Science*, 43(2):271–281, 2009.

(61) A. Delafargue and F.J. Ulm. Explicit approximations of the indentation modulus of elastically orthotropic solids for conical indenters. *International journal of solids and structures*, 41(26):7351–7360, 2004.

(62) R. Shahsavari, R.J.M. Pellenq, and F.J. Ulm. Empirical force fields for complex hydrated calcio-silicate layered materials. *Phys. Chem. Chem. Phys.*, 13(3):1002–1011, 2010.

(63) D. Alexander, J. Gee, and R. Bajcsy. Similarity measures for matching diffusion tensor images. In *Proceedings BMCV*, volume 99. Citeseer, 1999.

(64) V. Arsigny, P. Fillard, X. Pennec, and N. Ayache. Fast and simple calculus on tensors in the log-euclidean framework. *Medical Image Computing and Computer-Assisted Intervention–MICCAI 2005*, pages 115–122, 2005.

(65) M. Moakher. On the averaging of symmetric positive-definite tensors. *Journal of*

Elasticity, 82(3):273–296, 2006.

Figure Captions

Figure 1 : Mg-Mg radial distribution functions of two atomic structures used in simulations.

Figure 2 : Typical unit cell in periodic crystal of the simulated clay mineral at d=12Å.

Figure 3 : Change in average number of hydrogen bonds per water molecule and density of interlayer water during swelling of Wyoming Na-montmorillonite.

Figure 4 : Change in derivative of the density with respect to basal layer spacing during swelling of Wyoming Na-montmorillonite.

Figure 5 : Density profile of water oxygen(Ow) and water hydrogen(Hw) and sodium(Na) in direction normal to the clay layers.

Figure 6 : The C_{33} elastic constant as a function of basal layer spacing. Filled symbols represent data points from simulation (1) and hollow symbols represent data points from simulation (2). Triangular symbols represent equivalent transversely isotropic stiffness constants.

Figure 7 : The C_{44} and C_{55} elastic constants as a function of basal layer spacing. Legend as in Figure 6.

Figure 8 : The C_{13} and C_{23} elastic constants as a function of basal layer spacing. Legend as in Figure 6.

Figure 9 : The C_{11} and C_{22} elastic constants as a function of basal layer spacing. Legend as in Figure 6.

Figure 10 : The C_{12} elastic constant as a function of basal layer spacing. Legend as in Figure 6.

Figure 11 : Indentation modulus in z direction as a function of basal layer spacing. Legend as in Figure 6.

Figure 12 : Indentation modulus in the plane of transverse isotropy as a function of basal layer spacing. Legend as in Figure 6.

Figure 13 : (a) Relative Euclidean Metric as a function of basal layer spacing. (b) Riemannian Metric as a function of basal layer spacing. Legend as in Figure 6.
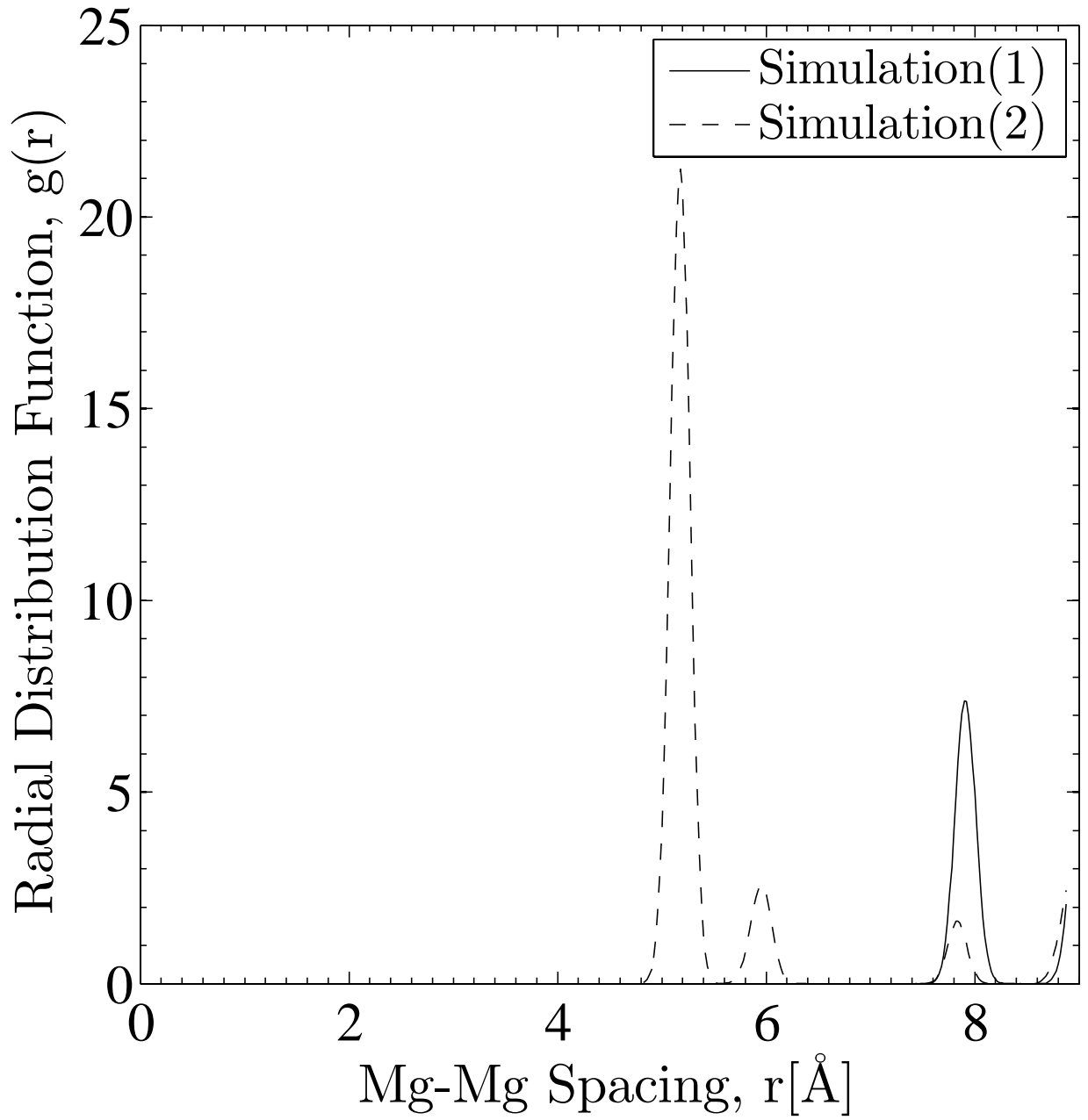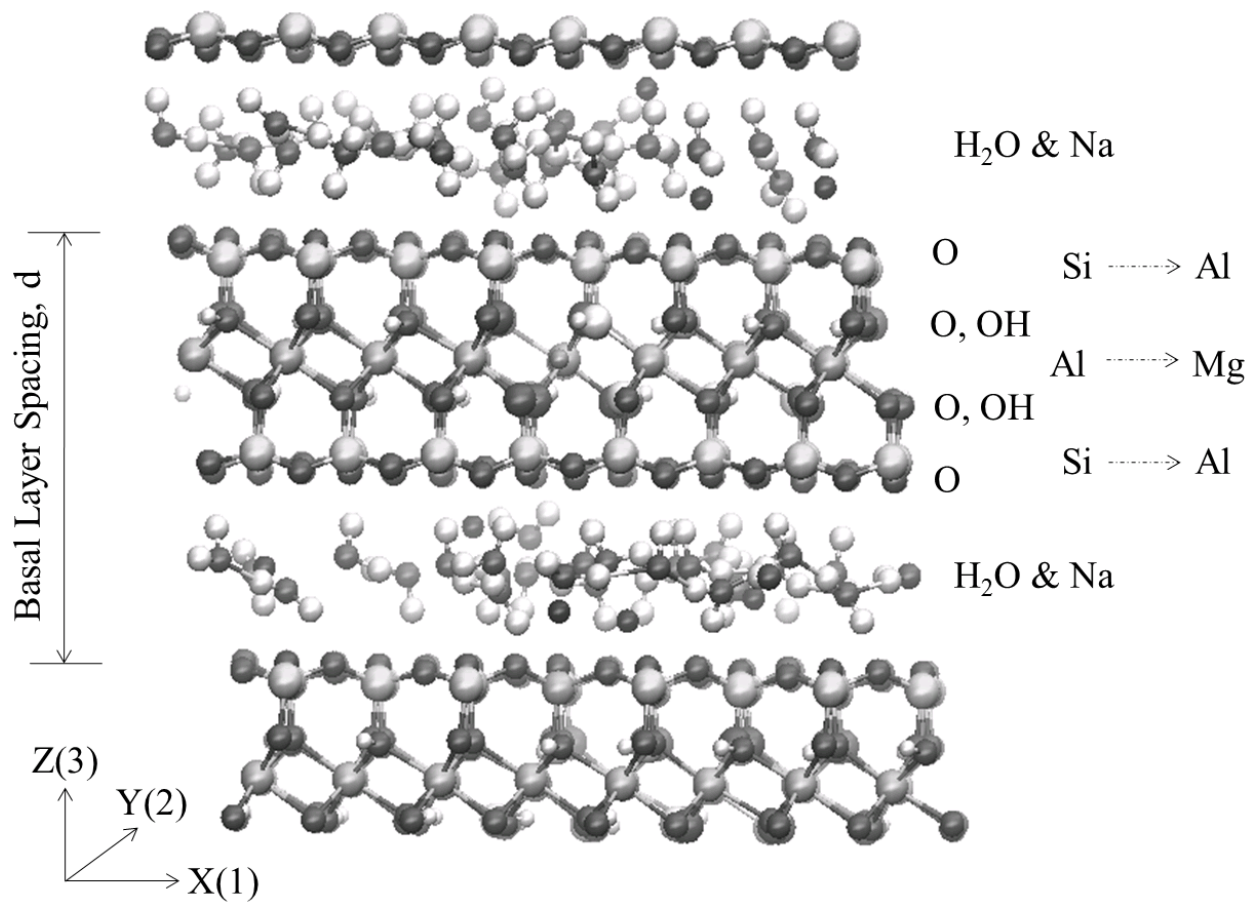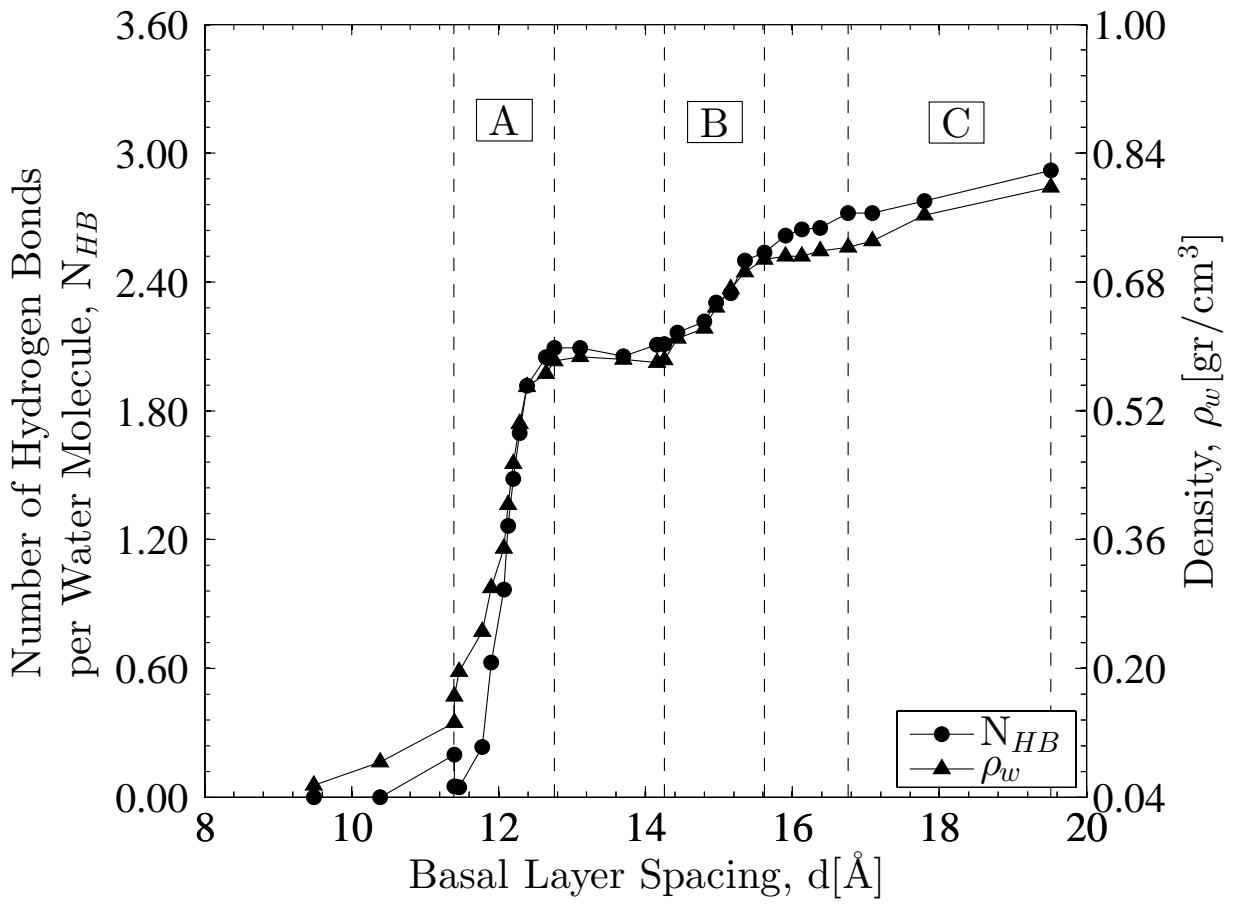
Figure 1

Figure 2

H₂O & Na

O   Si ------> Al

O, OH

Al ------> Mg

O, OH

O   Si ------> Al

H₂O & Na

Basal Layer Spacing, d

Z(3)
Y(2)
X(1)
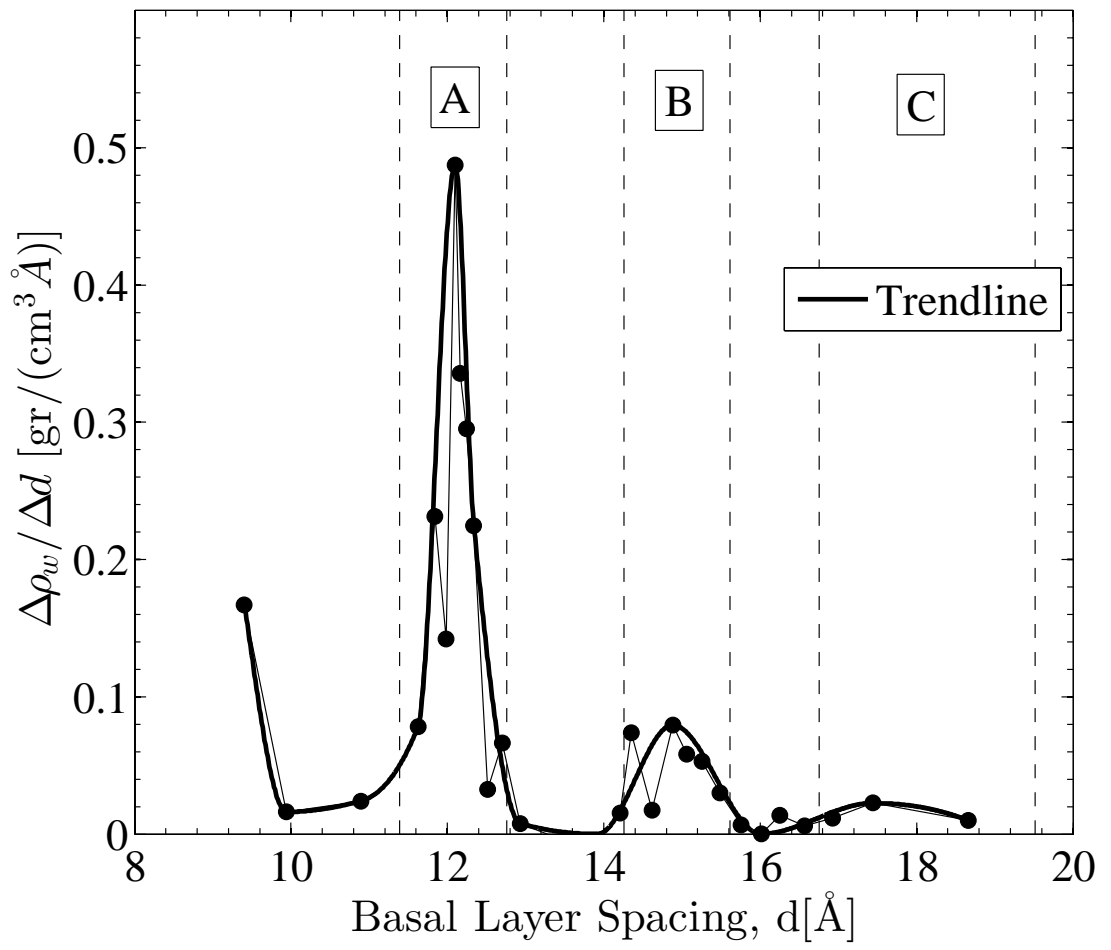
Figure 3

Figure 4

Figure 5
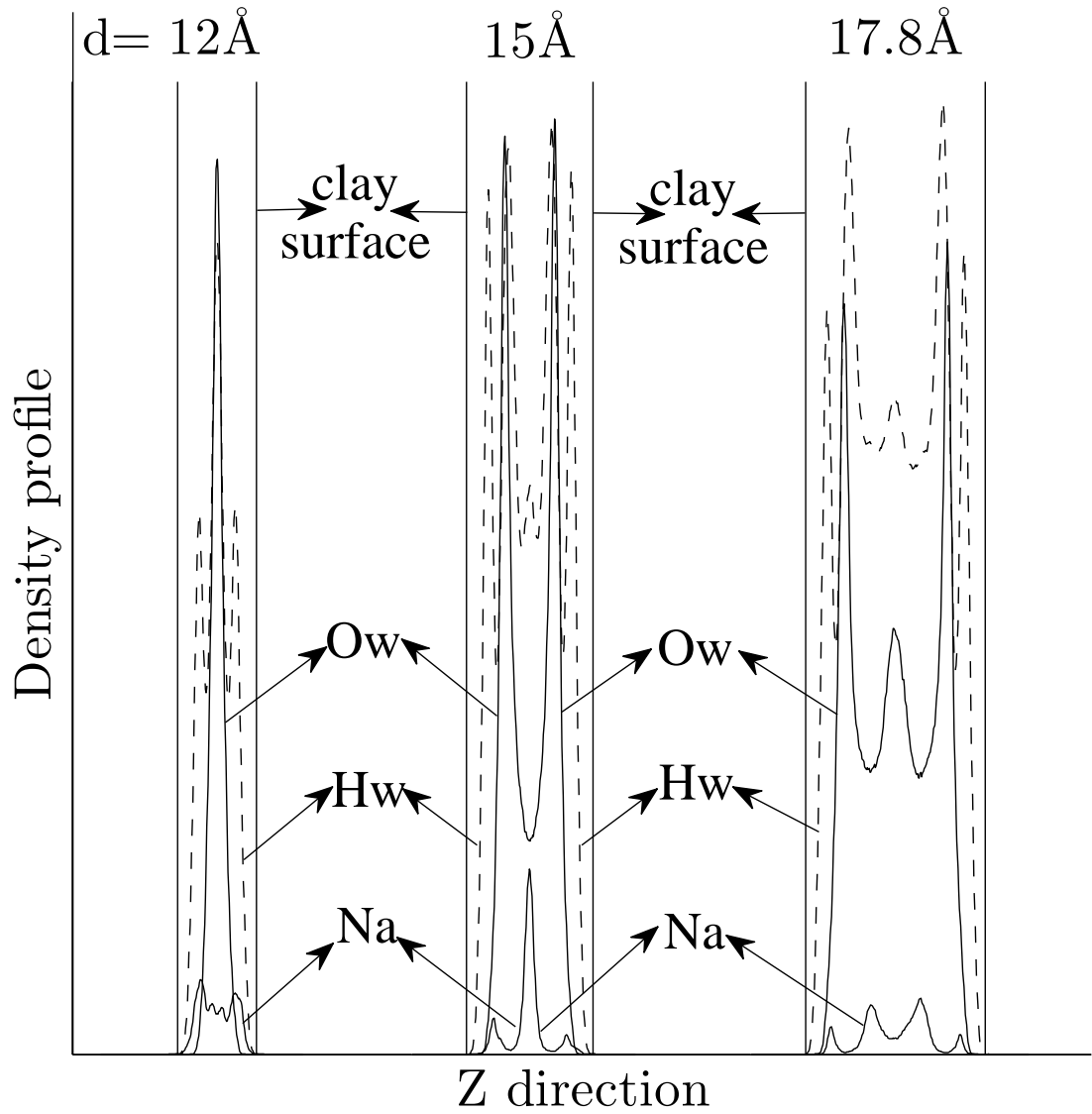
Figure 6
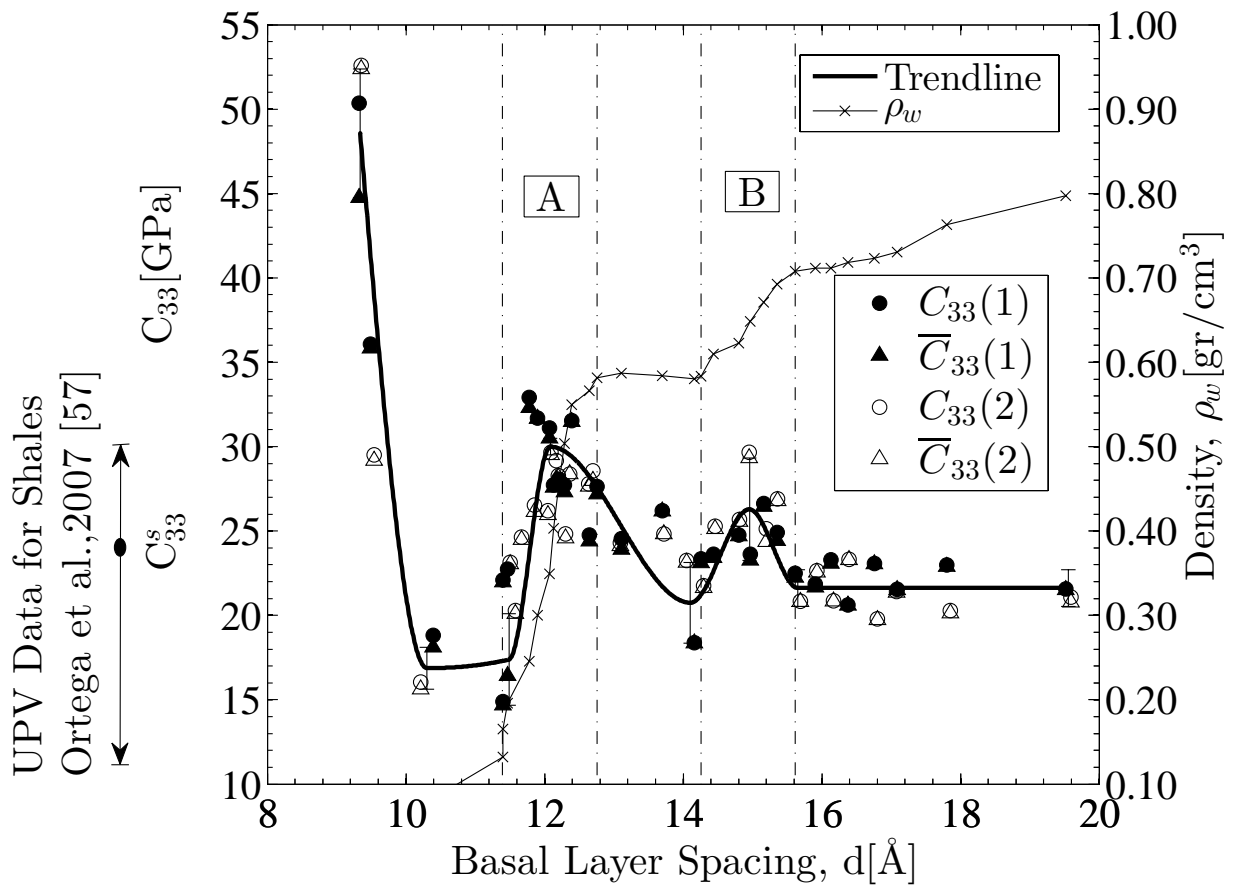
Figure 7
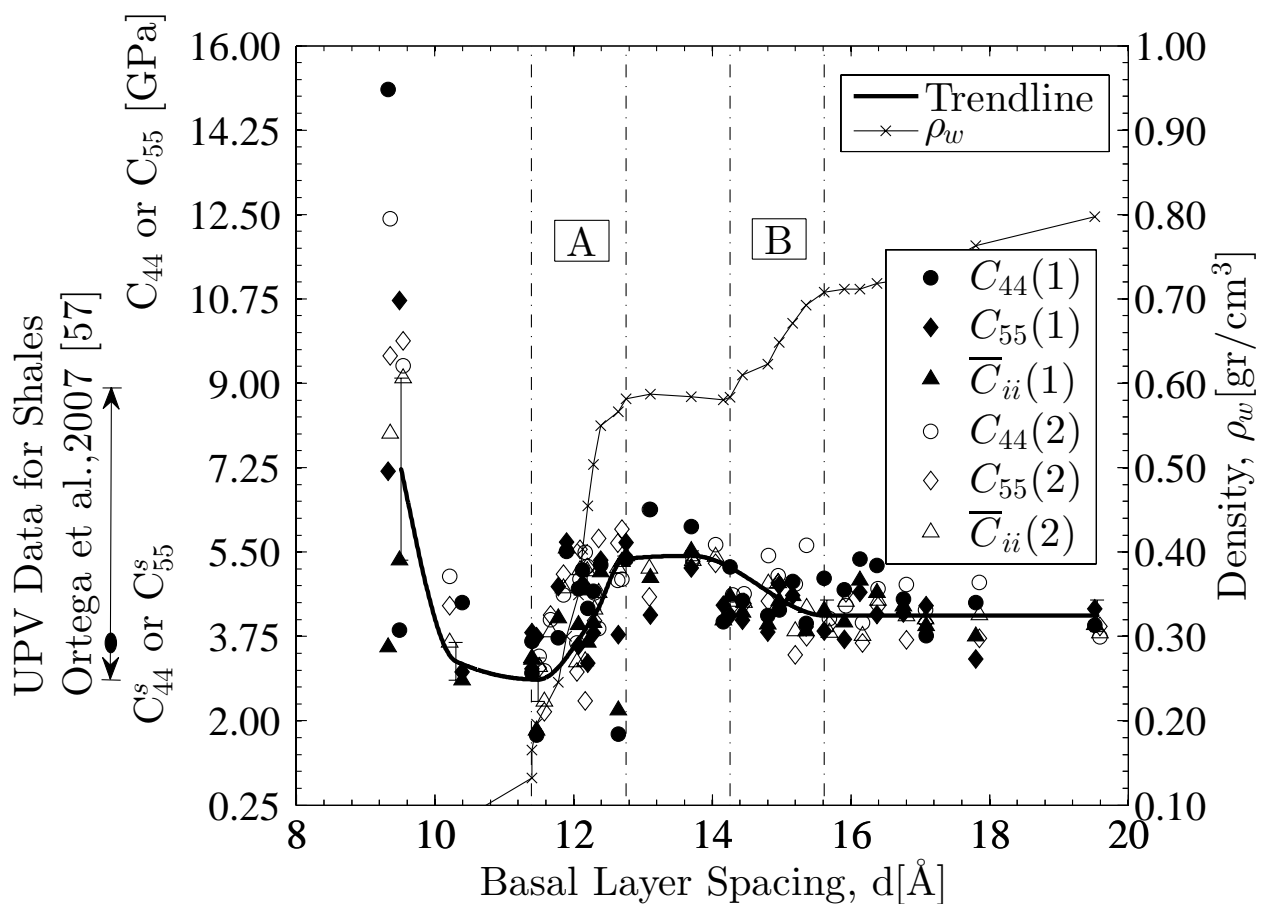
Figure 8
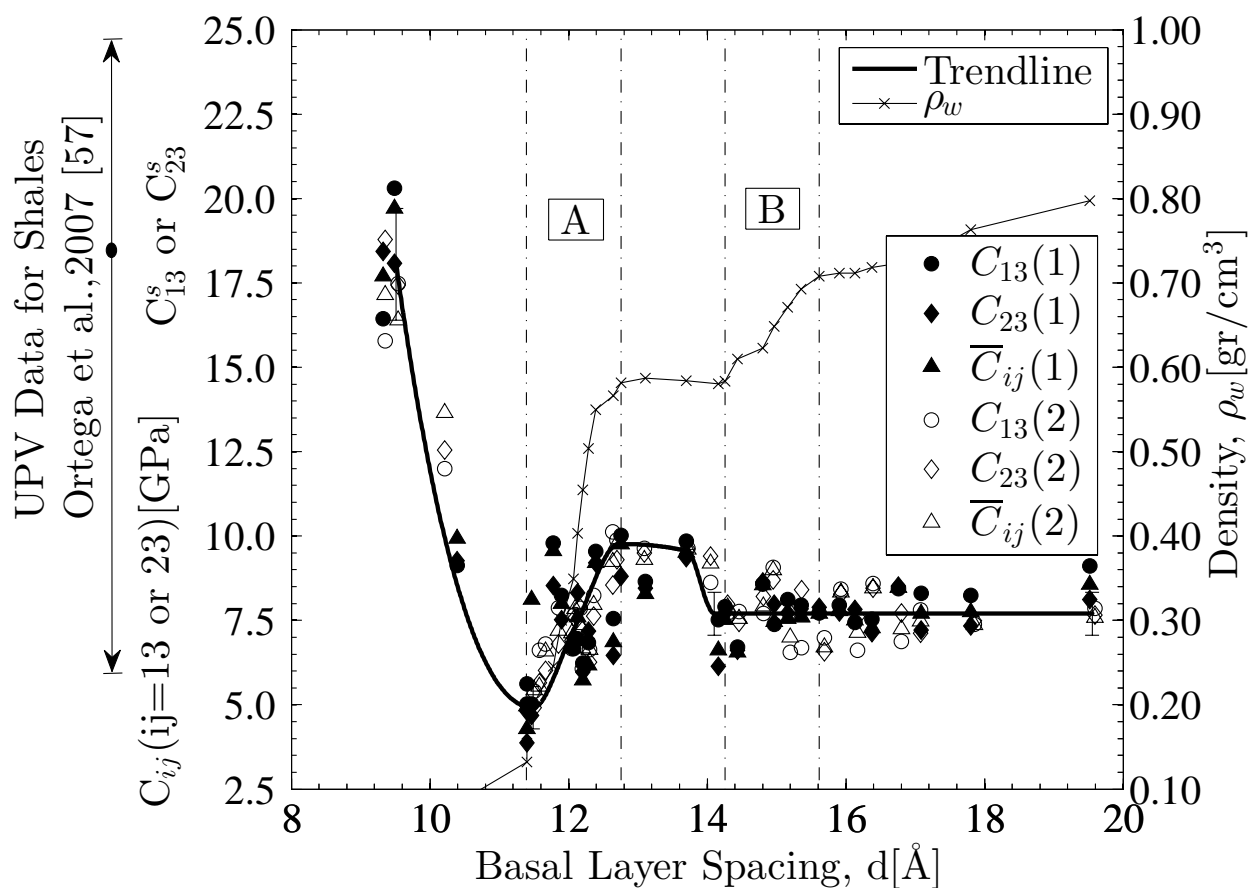
Figure 9

Figure 10
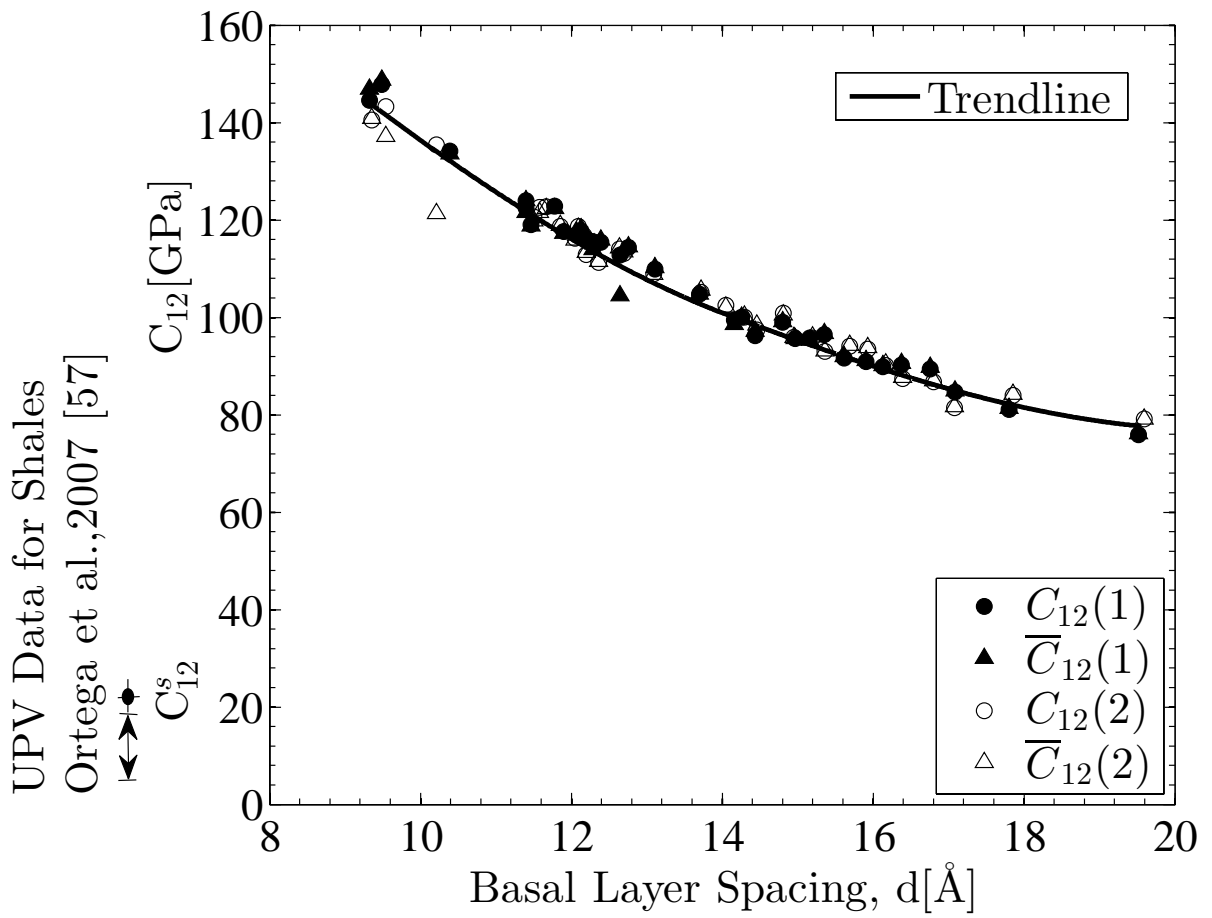
Figure 11

Figure 12

Figure 13

(a)

(b)